

Morphologies of three-dimensional shear bands in granular media

S. Fazekas^{1,2}, J. Török^{2,3}, J. Kertész², and D. E. Wolf⁴

¹*Theoretical Solid State Research Group of the Hungarian Academy of Sciences,*

²*Department of Theoretical Physics, and*

³*Department of Chemical Information Technology,
Budapest University of Technology and Economics,
H-1111 Budapest, Hungary*

⁴*Department of Physics, University Duisburg-Essen,
D-47048 Duisburg, Germany*

(Dated: February 20, 2006)

We present numerical results on spontaneous symmetry breaking strain localization in axisymmetric triaxial shear tests of granular materials. We simulated shear band formation using three-dimensional Distinct Element Method with spherical particles. We demonstrate that the local shear intensity, the angular velocity of the grains, the coordination number, and the local void ratio are correlated and any of them can be used to identify shear bands, however the latter two are less sensitive. The calculated shear band morphologies are in good agreement with those found experimentally. We show that boundary conditions play an important role. We discuss the formation mechanism of shear bands in the light of our observations and compare the results with experiments. At large strains, with enforced symmetry, we found strain hardening.

PACS numbers: 45.70.Cc, 81.40.Jj

Keywords: granular compaction, stress-strain relation

I. INTRODUCTION

The description of the rheological properties of dry granular media is a key question which controls the ability of handling (mixing, storing, transporting, etc.) of these particulate systems. An interesting and sometimes annoying feature of such materials is strain localization which appears almost always when a sample is subjected to deformation. The morphology of these narrow domains (shear bands) is far from being understood.

Two-dimensional and boundary induced shear band shapes have a vast literature dating back to decades including both numerical and experimental studies. Three-dimensional studies have a major drawback in the difficulty of getting information from inside the sample. However, in the past 20 years they gained increasing attention as experimental tools as Computer Tomography (CT) became available. Such experimental studies [1, 2, 3, 4] revealed complex localization patterns and shear band morphologies depending on the test conditions.

In this paper we focus on triaxial tests, which in general are elementary tests, performed to obtain mechanical properties of soils. The most common axisymmetric triaxial test consists of a cylindrical specimen enclosed between two end platens and surrounded by a rubber membrane on which an external pressure is applied (see for example [2]). The end platens are pressed against each other in a controlled way: Either with constant velocity (strain control) or with constant force (stress control). The force resulting on the platens or the displacement rate of the platens is recorded as well as the volume change of the specimen.

We report a numerical study of triaxial tests of cohesionless granular materials based on three-dimensional Distinct Element Method (DEM). We show that depend-

ing on the boundary conditions different shear band morphologies can be observed similar to experiments. We identify the shear bands by calculating the local shear intensity and show that it is correlated with the angular velocity of the particles and also with the local void ratio and the coordination number, which give alternative ways to detect shear bands and further verification of our results.

II. SIMULATIONS

We used a standard DEM with Hertz contact model [5] and appropriate damping [6] combined with a frictional spring-dashpot model [7, 8]. The triaxial tests were performed on vertical cylindrical samples (see Fig. 1) of diameter $D = 22 \text{ mm}$ and height $H = 46 \text{ mm}$ (i.e. the slenderness was $H/D \approx 2.1$ similar to most experiments). Each sample consisted of 27000 spherical particles with the same mass density $\rho = 7.5 \cdot 10^3 \text{ kg/m}^3$. The particles had a Gaussian size distribution. The mean particle diameter was $d = 0.9 \text{ mm}$. The standard deviation of the particle diameters was $\Delta d = 0.025 \text{ mm}$.

The normal F_n and tangential \mathbf{F}_t components of the contact force were calculated as

$$F_n = \kappa_n \delta_n^{3/2} - \gamma_n \delta_n^{1/2} v_n, \quad (1)$$

$$\mathbf{F}_t = \kappa_t \delta_t - \gamma_t \mathbf{v}_t, \quad (2)$$

where $\kappa_n = 10^6 \text{ N/m}^{3/2}$, $\kappa_t = 10^4 \text{ N/m}$, $\gamma_n = 1 \text{ N s/m}^{3/2}$, and $\gamma_t = 1 \text{ N s/m}$ are the normal and tangential stiffness and damping coefficients, δ_n and δ_t are the normal and tangential displacements, and v_n and \mathbf{v}_t are the normal and tangential relative velocities.

The normal displacement was calculated from the relative position, the size, and the shape of the bodies in

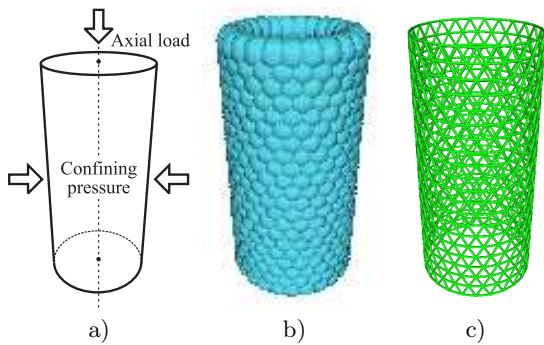


FIG. 1: (Color online) a) A granular sample was subjected to axial load and confining pressure. b) The rubber membrane surrounding the sample was simulated by overlapping spheres initially arranged in a triangular lattice. c) The neighboring spheres were interconnected with linear springs. The confining pressure acted on the triangular facets.

contact. The tangential displacement was calculated by integrating the tangential velocity in the contact plane during the lifetime of the contact. The Coulomb law limits the (tangential) friction force to μF_n (where $\mu = 0.5$ is the used coefficient of friction). To allow for sliding contacts, we limited the length of the tangential displacement to $\mu F_n / \kappa_t$. (For a review on DEM see [7, 8] and references therein. For more details on our implementation see [9].)

The translational motion of bodies is calculated with Verlet’s leap-frog method. The rotational state is integrated in quaternion representation with Euler’s method. With the above stiffness and damping coefficients, the inverse of the average eigenfrequency of contacts, in both normal and tangential direction, is more than one order of magnitude larger than the used integration time step $\Delta t = 10^{-6}$ s. This assures that the noise level induced by numerical errors and grain elasticity is kept low.

The initial configuration was generated by randomly placing the grains in a tall solid cylinder having height $h = 3H$ and width D . The maximum allowed initial grain overlap was 1%. The upper platen and the particles were given downward velocities $v \propto z/h$ depending on their vertical position z measured from the fixed bottom platen. These conditions lead to an almost simultaneous first contact of the bodies. The system was stabilized with a force applied on the upper platen. This was switched on when the inner pressure of the sample could compensate it. In preparation (and later in the tests) we used zero gravity. The deposition method described above is known to produce a homogeneous system. During the preparation phase, the friction of the particles was switched off to allow for generation of dense samples. (For a review on sphere packings see [10].)

The solid cylinder used in preparation was replaced by an *elastic membrane* in the tests. The elastic membrane was modeled with overlapping spheres having equal diameter $d_m = 1$ mm and equal mass density $\rho_m =$

100 kg/m^3 , and initially forming a triangular lattice on the external surface of the cylinder. The “membrane nodes” could not rotate and were interconnected with linear springs having an elongation equal to the relative distance of the nodes (initially 0.5 mm). The stiffness of the springs $\kappa_s = 0.5 \text{ N/m}$ was chosen such that the particles could not escape by passing through the membrane. Additionally a homogeneous confining pressure $\sigma_c = 500 \text{ N/m}^2$ was applied on the membrane. This was simulated by calculating the forces acting on the triangular facets formed by connected membrane nodes.

A similar model was used by Tsunekawa and Iwashita [11] who applied the confining pressure directly on the external particles in a very similar way. However, their approach requires the computationally expensive identification of external particles and a Delaunay triangulation. Sakaguchi and Mühlhaus [12] used a similar membrane model to ours but without an explicit confining pressure, relying only on the stiffness of the springs.

The bottom platen was fixed during both preparation and test phases. The upper platen could not tilt in preparation phase, but in certain tests it could freely tilt along any horizontal axis with rotational inertia $I = 10^{-7} \text{ kg m}^2$. During the tests, the samples were compressed by moving the upper platen in vertical direction downwards with a constant velocity (strain control). Starting from the same initial condition, four different runs – denoted by (A), (B), (C), and (D) – were executed. Two different compression velocities were used: A base value $u_1 = 10 \text{ mm/s}$ (in tests (A) and (B)) and a two times larger value $u_2 = 2u_1$ (in tests (C) and (D)). Tilting of the upper platen was enabled in tests (A) and (C) and disabled in tests (B) and (D).

III. RESULTS

A. Local shear intensity

We define the local shear intensity S by generalizing its two-dimensional definition given by Daudon et al. [13]. First, the regular triangulation [14] of the particle system is calculated [15]. The displacements of the particles (relative to a previous state) are known from the DEM simulation. We extend the displacement field to the whole volume of the sample with a linear interpolation over the tetrahedra of the regular triangulation. For each particle we identify the incident triangulation cells (tetrahedra) which define a discrete particle neighborhood. The particles at the sample’s boundary, having infinite incident cells, are skipped (i.e. no local shear intensity is defined for them). The discrete neighborhood of a particle is a surrounding polyhedron with first-neighbor particles at the corners.

We define the deformation gradient tensor with the partial (space) derivatives $\partial_i u_j$ of the displacement vector \mathbf{u} . In a neighborhood Ω of volume V , the components of

the mean deformation gradient tensor are calculated as

$$\langle u_{ij} \rangle = \frac{1}{V} \int_{\Omega} \partial_i u_j dV. \quad (3)$$

Using the Gauss-Ostrogradski theorem the volume integral can be transformed into a closed surface integral over the boundary $\partial\Omega$ of Ω , leading to

$$\langle u_{ij} \rangle = \frac{1}{V} \oint_{\partial\Omega} n_i u_j dS, \quad (4)$$

where \mathbf{n} is the exterior normal along the boundary. We calculate the local deformation gradient tensor applying the above formula to discrete neighborhoods and using the linear interpolation of the particle displacements. In this case the integral can be reduced to a summation over triangular facets.

The symmetric part of the local deformation gradient tensor is a macroscopic strain tensor derived from particle displacements. Using the eigenvalues ε_k of this macroscopic strain tensor, we define the local shear intensity as

$$S = \max_k \left| \varepsilon_k - \frac{1}{3} \sum_l \varepsilon_l \right|. \quad (5)$$

We note that we disregard the elastic deformation and rotation of the grains, since we are interested in the identification of the shear bands, which is strongly linked to geometric effects. However, for constitutive models, a more complete treatment of the strain would be needed [16].

B. Shear band morphologies

Taking cross sections of the sheared samples and coloring the grains according to the local shear intensity S , we could identify shear bands (see Fig. 2) and compared them with experiments. In experiments the CT scans show the volume fraction difference between the bulk and the shear band. In the next section we justify the comparison of the volume fraction and local shear intensity.

Our simulations are run at zero gravity and low confining pressure in very similar conditions to the experiments of Batiste et al. [3]. The shear band patterns found in their experiments and our simulations are also very close to those found in experiments under normal gravity and high confining pressure by Desrues et al. [2], who also studied the case of a tilting upper platen. We compared our results to both experiments.

We found that the absence of enforced axisymmetry leads to spontaneous symmetry breaking. When tilting of the upper platen is enabled internal instabilities can develop into a localized deformation along a failure plane (see panel (c) of Fig. 2). Non-tilting platens act as a stabilizing factor leading to an axisymmetric hourglass

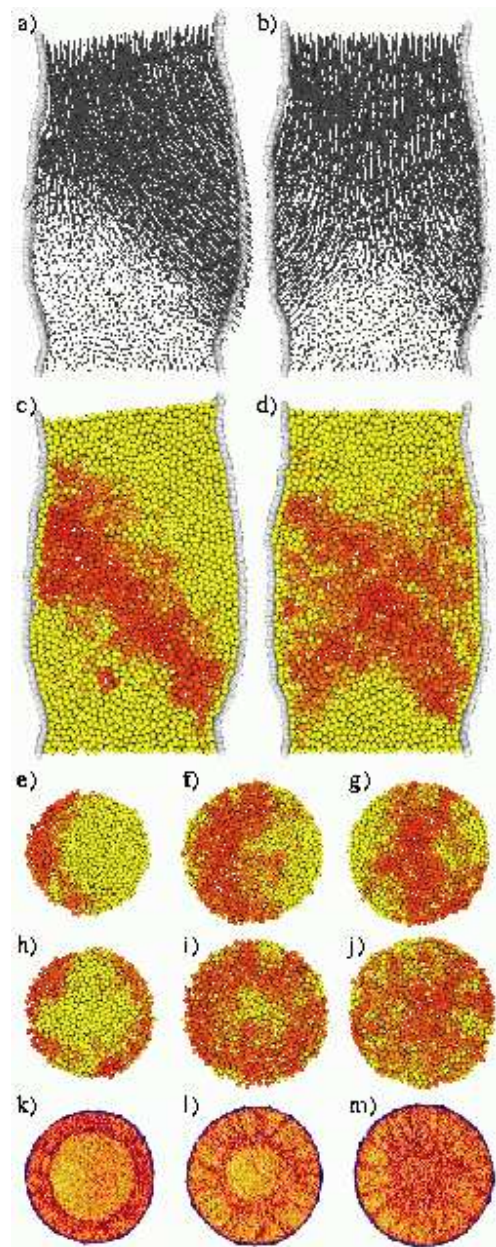


FIG. 2: (Color online) Cross sections (a, c, e, f, g) of sample (C) and cross sections (b, d, h, i, j) of sample (D) shown at 10% axial strain. Panels (k, l, m) present CT scans [3] (F2075). The vertical cross sections (a-d) were taken at the middle of the sample. The horizontal cross sections were taken at different heights: close to the top (e, h, k), at the middle (g, j, m), and in between (f, i, l). The red color encodes the local shear intensity on panels (c-j) and the local void ratio on panels (k-m). Panels (a, b) show the velocity field.

shaped shear band with two conical surfaces and complex localization patterns around them (see panel (d) of Fig. 2). This is in full accordance with the experimental results of Desrues et al. [2]. For the non-tilting case Tsunekawa and Iwashita [11] found in DEM simulations similar localization patterns, however they have not in-

vestigated the tilting case.

In the non-tilting case, the horizontal cross sections (h, i, j) shown on Fig. 2 can be compared with the experimental results of Batiste et al. [3]. They reported the same type of shear band morphologies for these boundary conditions. The panels (k, l, m) of Fig. 2 show CT scans from their triaxial shear tests executed in micro-gravity aboard a NASA Space Shuttle. Our simulations used similar setup and similar confining pressure. Good agreement of shear band shapes (including their non-trivial structure) can be recognized in spite of the rather limited number of grains in our simulations. (Note that the details reproduce better in the color version of the figure.)

In the case of tilting upper platen the shear bands are not totally plane – as can be seen on horizontal cross sections taken close to the platens – but follow the curvature of the boundary. The same was found experimentally by Desrues et al. [2]. In the vertical cross sections shown on the panels (c) and (d) of Fig. 2, the found shear bands are in good agreement with changes in the velocity field shown on panels (a) and (b). This justifies the shear band identification method based on the local shear intensity. We have also investigated alternative methods.

C. Alternative methods of shear band identification

It is widely known that dense granular materials dilate during shear. In some experiments (e.g. experiments based on CT [2, 3]) the local void ratio is used to identify the shear bands. To confirm the presented shear band identification method and the found shear band morphologies, we have investigated the correlation between the local void ratio ν and the local shear intensity S . The void ratio was measured using the regular triangulation [14, 15] of the spherical particles. The volume of the regular Voronoi cells V_c and the volume of the grains V_g define the local void ratio $\nu = (V_c - V_g)/V_g$.

In numerical simulations (for spheres of nearly equal size), a good alternative to the local void ratio ν is the coordination number Z (defined by the number of contacts), which decreases as ν increases. Its main advantage is that it can be defined exactly and calculated fast, however, if the size distribution is wide a non-trivial particle size scaling has to be taken into account.

The existence of particle rotations in shear bands is known to experimentalists for a long time (see e.g. [17]). It was also evidenced in simulations by Herrmann et al. [18]. In our simulations, we have also measured for each grain the absolute value of the angular velocity R and tested its correlation with the local shear intensity S .

All the quantities mentioned above (the local void ratio ν , the coordination number Z , the angular velocity R , and the local shear intensity S) are defined for each particle. We checked their correlation with a histogram technique using the values calculated for different particles as different statistical samples. The ν , Z , and R values were averaged for each (logarithmic) histogram bin

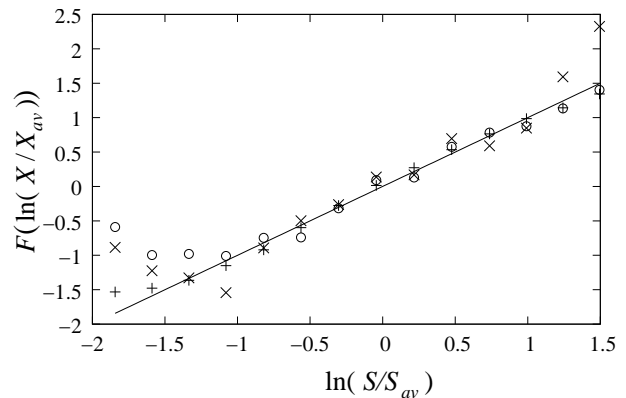


FIG. 3: Correlation of the local shear intensity S with the local void ratio (ν , \circ), the coordination number (Z , \times), and the angular velocity of the grains (R , $+$). X is one of ν , Z , and R . F denotes a linear transformation different for each data set. All quantities are scaled by average values (X_{av} , S_{av}). The data is collected from four samples at 10% axial strain. See text for more details.

of S . We also calculated the total averages ν_{av} , Z_{av} , R_{av} , and S_{av} . On the quantities $\xi = \ln(X/X_{av})$ (where X is one of ν , Z , and R) we applied different linear transformations $F(\xi) = \alpha(\xi - \xi_0)$ (shift and scaling) to achieve data collapse of $F(\ln(X/X_{av}))$ as function of $\ln(S/S_{av})$ (see Fig. 3).

The scaling term α of F shows the sensitivity of the R , Z , and ν quantities with respect to the local shear intensity S . We found $\alpha = 1$ for the angular velocity, $\alpha = -9$ for the coordination number, and $\alpha = 27$ for the local void ratio. (Note that Z decreases as S increases!) The fluctuations were proportional to $\sqrt{|\alpha|}$. Regarding shear band identification, this means that the angular velocity is essentially equivalent with the local shear intensity. However, the coordination number and the local void ratio are less sensitive, and they exhibit large fluctuations due to random packing and random rearrangements. For this reason they need more spatial and/or temporal averaging to achieve the same accuracy.

D. Stress-strain relation

In order to compare to most common experimental results, we measured the stress σ on the upper platen, and calculated the stress ratio σ/σ_0 , where σ_0 denotes the initial stress. As the axial strain increases, the response of the granular sample (the stress ratio) increases until it reaches a peak value, then it decreases (see Fig. 4). According to Fig. 4, up to 15% axial strain there is no significant difference in stress-strain relation measured in different simulation runs, indifferent to strain rate and tilting of the upper platen. (We have not tested dependence on material parameters and confining pressure.)

The presented strain softening effect is a basic observation of triaxial shear tests of dense granular specimens

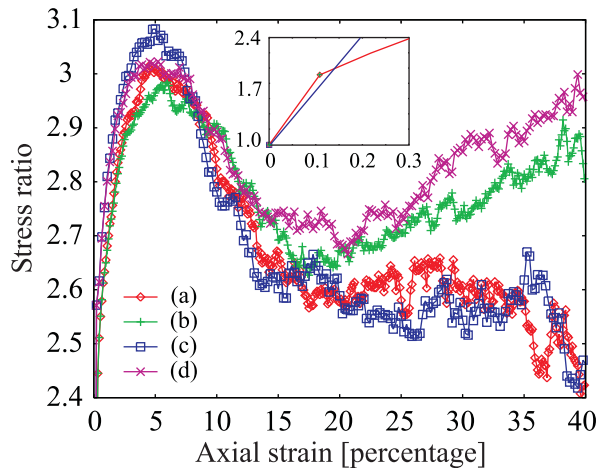


FIG. 4: (Color online) Stress-strain relation. The stress ratio σ/σ_0 (where σ_0 denotes the initial stress) measured on the upper platen is shown as function of the axial strain, for different simulation runs. (See inset for low strains.) For the lower two curves (a, c) tilting of the upper platen was enabled, and for the upper two (b, d) it was disabled. For (c, d) the samples were compressed two times faster than for (a, b).

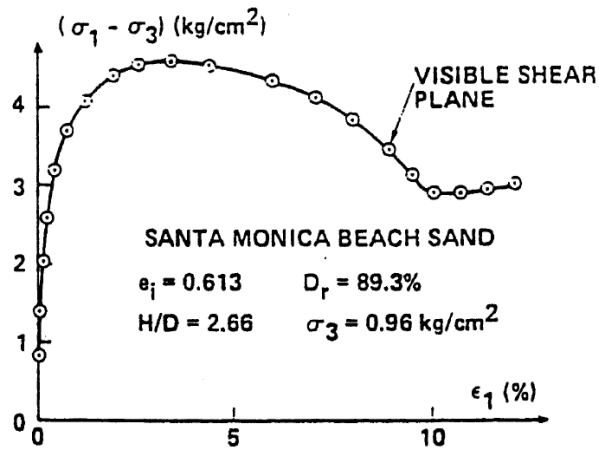


FIG. 5: Experimental stress-strain relation from a triaxial compression test exhibiting strain softening and development of shear plane. (Courtesy of Poul V. Lade, Reprinted from [19] with permission from Elsevier.)

(see for example [19] and Fig. 5). Any local deformation due to shear is followed by a dilatation resulting in a decrease of the force bearing capacity of the material which further intensifies the deformation leading to failure. In our simulations we observed pronounced shear bands around 10% axial strain, which is in good agreement with the experimental results.

After about 15% axial strain the different boundary conditions and shear band shapes result in different stress-strain curves. In the non-tilting case, the geometry and the hourglass-shaped shear band forces the particles to enter and leave the failure zone. In this case, a stable

slipping mode cannot be formed. As the test sample is further compressed, it opposes more and more firmly to compression (see curves (b) and (d) on Fig. 4), resulting in increasing stress ratio (i.e. strain hardening). In the tilting case, the upper part of the sample moves as a single block. The formed planar shear band allows for a stable slipping mode with nearly constant stress until boundary effects come into play (see curves (a) and (c) on Fig. 4).

IV. CONCLUSIONS

Triaxial shear test simulations based on DEM were executed and different shear band morphologies known from experiments were reproduced [21]. We have shown that in triaxial shear tests symmetry breaking strain localization can develop spontaneously if the axial symmetry is not enforced by non-tilting platens. To our knowledge it is the first time that such symmetry breaking strain localization was reproduced in DEM simulations.

We generalized the shear intensity definition of Daudon et al. [13] to three-dimensions and used it to identify shear bands. To be able to compare to experiments, we have also tested alternative methods of shear band identification. We found strong correlation of the local shear intensity with the angular velocity of the grains, the coordination number, and the local void ratio. This result justifies our method and proves once more the known experimental and numerical findings that shear bands are characterized by dilation and rotation of the grains. Regarding shear band identification, the coordination number and the local void ratio are found to be less sensitive than the local shear intensity and the angular velocity of the grains.

We have also measured the stress-strain relation of the compressed samples. Strain softening was identified in good agreement with experimental results. We have also found a strain hardening effect at large strains in the non-tilting case and explained it in terms of geometry and shear band morphology. However, this might be only valid for the tested material parameters and confining pressure. We have no knowledge of experiments focusing on this particular question. In general, the agreement of our results with the experimental results is very good, even if the system size (number of particles) in our simulations is much smaller than in experiments.

V. ACKNOWLEDGMENTS

This research was carried out within the framework of the “Center for Applied Mathematics and Computational Physics” of the BUTE, and it was supported by BMBF, grant HUN 02/011, and Hungarian Grant OTKA T035028, F047259.

-
- [1] J. Desrues, R. Chambon, M. Mokni, and F. Mazerolle, *Géotechnique* **46**, 529 (1996).
 - [2] J. Desrues, in *X-ray CT for Geomaterials*, edited by J. Otani and Y. Obara (Balkema, 2004), pp. 15–41.
 - [3] S. N. Batiste, K. A. Alshibli, S. Sture, and M. Lankton, *Geotechnical Testing Journal* **27**, 568 (2004).
 - [4] K. A. Alshibli, S. Sture, N. C. Costes, M. L. Frank, M. R. Lankton, S. N. Batiste, and R. A. Swanson, *Geotechnical Testing Journal* **23**, 274 (2000).
 - [5] L. D. Landau and E. M. Lifshitz, *Theory of Elasticity* (Pergamon, New York, 1970), chap. 9, (2nd English ed.).
 - [6] N. V. Brilliantov, F. Spahn, J.-M. Hertzsch, and T. Pöschel, *Phys. Rev. E* **53**, 5382 (1996).
 - [7] S. Luding, in *The Physics of Granular Media*, edited by H. Hinrichsen and D. E. Wolf (Wiley-VCH, Weinheim, 2004).
 - [8] T. Pöschel and T. Schwager, *Computational Granular Dynamics: Models and Algorithms* (Springer, Berlin, 2005).
 - [9] S. Fazekas, J. Török, J. Kertész, and D. E. Wolf, in *Powders and Grains 2005*, edited by R. García-Rojo, H. J. Herrmann, and S. McNamara (Balkema, London, 2005), pp. 223–226.
 - [10] D. A. Weitz, *Science* **303**, 968 (2004).
 - [11] H. Tsunekawa and K. Iwashita, in *Powders and Grains 2001*, edited by Y. Kishino (Balkema, 2001), pp. 177–180.
 - [12] H. Sakaguchi and H.-B. Mühlhaus, in *Exploration Geodynamics Chapman Conference* (American Geophysical Union, 2001), pp. 153–155.
 - [13] D. Daudon, J. Lanier, and M. Jean, in *Powders and Grains 1997*, edited by Behringer and Jenkins (Balkema, 1997), pp. 219–222.
 - [14] C. Lee, in *Applied Geometry and Discrete Mathematics: The Victor Klee Festschrift*, edited by P. Gritzmann and B. Sturmfels (American Mathematical Society, Providence, RI, 1991), pp. 443–456.
 - [15] CGAL, <http://www.cgal.org>, Computational Geometry Algorithms Library (CGAL 2.4) (2003).
 - [16] C. O’Sullivan, J. D. Bray, and S. Li, *Int. J. Numer. Anal. Meth. Geomech.* **27**, 859 (2003).
 - [17] M. Oda and H. Kazama, *Geotechnique* **48**, 465 (1998).
 - [18] H. J. Herrmann, J. A. Astrom, and R. M. Baram, *Physica A* **344**, 516 (2004).
 - [19] P. V. Lade, *International Journal of Solids and Structures* **39**, 3337 (2002).
 - [20] M. J. Jiang, H. S. Yu, and D. Harris, *Computers and Geotechnics* **32**, 340 (2005).
 - [21] We have ignored the rolling resistance (see e.g. [20]) in these calculations. Our simulations demonstrate that this effect is not crucial in the qualitative description of tri-axial shear tests.